PAPER • **OPEN ACCESS**

An integrated hybrid 3D bioprinting of heterogeneous and zone-specific construct resembling structural and biofunctional properties of osteochondral tissue

To cite this article: Yaxin Wang *et al* 2025 *Mater. Futures* **4** 025401

OPEN ACCESS
IOP Publishing | Songshan Lake Materials Laboratory

MATERIALS FUTURES

Mater. Futures 4 (2025) 025401 (19pp) https://doi.org/10.1088/2752-5724/adb7f6

An integrated hybrid 3D bioprinting of heterogeneous and zone-specific construct resembling structural and biofunctional properties of osteochondral tissue

Yaxin Wang[1], Yanhao Hou[1], Cian Vyas[2,*], Boyang Huang[2,*] and Paulo Bartolo[2,*]

[1] Department of Mechanical and Aerospace Engineering, University of Manchester, Manchester M13 9PL, United Kingdom
[2] Singapore Centre for 3D Printing, Nanyang Technological University, Singapore 639798, Singapore

E-mail: cian.vyas@ntu.edu.sg, boyang.huang@ntu.edu.sg and pbartolo@ntu.edu.sg

Received 3 August 2024, revised 13 February 2025
Accepted for publication 19 February 2025
Published 3 March 2025

Abstract

Extrusion-based 3D printing is extensively used to fabricate osteochondral (OC) constructs. However, significant challenges remain, particularly engineering constructs that can replicate the heterogeneity and structural organization of OC tissue and maintain a chondrogenic phenotype. Herein, this study introduces an integrated hybrid 3D bioprinting strategy, incorporating soft hydrogel bioinks and a bioceramic thermoplastic composite polymer, allowing the fabrication of a zone-specific construct analogous to OC tissue. The results show that the hybrid triphasic 3D bioprinted construct mimicking the full-thickness OC tissue displays a distinct layered structure with high precision and improved mechanical properties. The calcified layer fabricated by co-printing gelatin methacryloyl (GelMA) and polycaprolactone/tricalcium phosphate (PCL/TCP) enables the formation of a transition layer and provides strong bonding between the engineered PCL/TCP subchondral bone and the methacrylated methylcellulose (MCMA)/GelMA cartilage layer. The encapsulated human adipose-derived stem cells are found to be spatiotemporally released from the calcified cartilage layer and directionally attach to the subchondral bone layer of the construct. The MCMA/GelMA bioinks exhibit a stiffness and stress relaxation profile suitable for cartilage applications. Human chondrocytes (HCs) show enhanced cell viability and proliferation. Moreover, the HCs encapsulated within the MCMA/GelMA bioinks maintain their chondrogenic phenotype with high expression of collagen type II (Col2) and SOX9. At the liquid-matrix interface, they experience a loss of chondrogenic phenotype and potential chondrogenic-to-osteogenic trans-differentiation with the expression of the osteogenic marker

* Authors to whom any correspondence should be addressed.

collagen type I (Col1). This study provides a deep understanding and insightful view of chondrogenic behaviours responding to the microenvironment via extensive *in-vitro* studies and shed light on a promising approach for the future OC tissue regeneration.

Supplementary material for this article is available online

Keywords: 3D bioprinting, biomaterials, bioinks, cartilage, osteochondral tissue

1. Introduction

Osteochondral (OC) tissue exhibits a heterogeneous and hierarchical organisation comprising articular cartilage, an interface layer of calcified cartilage, and subchondral bone, in an approximate proportion of 90%, 5%, and 5% [1]. The tissue is crucial for the functioning of synovial joints and facilitates bodily movement. Compressive forces transferred from the soft cartilage to the hard bone minimise fatigue damage to the OC tissue over a lifetime of cyclic loads [2]. However, cartilage has limited self-regeneration due to the avascular and aneural composition of the tissue and limited metabolic activity of chondrocytes. Subsequently, cartilage defects that progress to the subchondral bone region result in the development of osteoarthritis. Currently there are limited efficacious therapeutic options and ultimately a joint replacement may be required in severe cases. Moreover, the incomplete restoration of the OC defect limits the long-term functionality of the joint [3]. Therefore, there is an unmet need to fabricate an engineered scaffold for OC repair and regeneration. However, the diverse properties of the OC tissue, considering the biochemical and biomechanical properties, cellular composition, and the organised functional gradient results in a significant challenge.

Tissue engineering combining 3D printing, biomaterials, and cells has been widely explored to fabricate constructs mimicking the physiological, hierarchical, and anatomical structure of OC tissue [4–7]. A commonly used strategy is to fabricate bilayered scaffolds exhibiting distinct phases in a single structure, mimicking the cartilage and subchondral bone regions [8–14]. However, bilayered constructs are unable to recapitulate the complex functional gradient structure of OC tissue. Moreover, the abrupt changes in mechanical properties between the two phases result in a weak interface and poor integration. Gu *et al* [13] mitigated this by using a precisely patterned porous bilayered gelatin methacryloyl (GelMA) construct to improve layer integration via the use of a mono-material and specifically guide cell migration. However, the calcified cartilage interface as a transition layer isolating the microenvironment of the two phases was not included and is typically neglected in bilayered constructs. Furthermore, the lack of distinct cell-instructive material environments for each region limits the biomimicry of the construct. Therefore, triphasic or multiphasic scaffolds have been developed, allowing a smoother phase transition between the distinct zones in terms of mechanical properties and the cell and extracellular matrix (ECM) composition [1, 6, 15, 16]. Nevertheless, this leads to an increased complexity of the manufacturing process, requiring, for instance, the combination of multiple printing techniques and crosslinking procedures [5, 17]. Extrusion-based 3D printing shows a unique advantage of heterogeneity among other 3D printing techniques, allowing integration of different materials in the same construct or within the same layer by alternatively using multiple printheads [18, 19]. For example, Chae *et al* [16] have bioprinted a tendon-bone interface construct for rotator cuff repair using a gradient of region specific decellularised ECM bioinks to direct the differentiation of encapsulated human bone marrow mesenchymal stem cells (MSCs). However, a challenge remains in the fabrication of complex multi-cellular OC constructs and the precise delivery and confinement of multiple cell types to specific regions. This is especially relevant in maintaining the specific zonal lineages with OC tissue and preventing loss of the desired phenotype. Moreover, the use of manual cell seeding of a scaffold or tissue construct to introduce additional cell types is imprecise and associated with an inhomogeneous cell distribution [20, 21].

OC tissue comprises a hard tissue (subchondral bone), an intermediate calcified region, and a softer tissue phase (cartilage). Considering the zonal specific features, the integration of chondrogenic and osteogenic cell lineages into a single construct would be ideal for the reconstruction of the OC tissue. Subsequently, a potential strategy is to fabricate a cell-laden triphasic construct using extrusion-based bioprinting including an engineered multi-functional calcified cartilage intermediate layer. This transition layer provides a gradient between the bone and cartilage region but also a physical barrier. This can enable cell confinement to their specific regions and limit cellular crosstalk. The interface between the calcified intermediate layer and the cartilage region can be used to maintain an avascular environment, chondrocyte phenotype, and low oxygen levels, within the cartilage, thus enhancing the chondrogenesis [22–24]. Furthermore, a cell-laden calcified cartilage intermediate layer can be further developed into an *in-situ* directional cell release layer to provide cells for not only the calcified cartilage region but as a cell bank for the bone region. This can be achieved by incorporating MSCs as they have the capacity to differentiate into both osteogenic and chondrogenic lineages [25–28]. The cell carriers and microenvironment should be carefully designed to provide instructive cues to guide differentiation towards the separate osteogenic and calcified cartilage phenotypes. Therefore, it is highly

relevant to develop a simple extrusion-based 3D bioprinting strategy, allowing an OC construct with structurally integrated and biofunctional heterogeneous layers analogous to the anatomical native OC regions.

In our previous work, we have demonstrated that 3D polycaprolactone (PCL) and tricalcium phosphate (TCP) scaffolds show satisfying mechanical properties and regulate osteogenic behaviour via mechanotransduction pathways [29]. However, additional cell seeding steps after the printing process are required due to the high melting temperature, leading to an inhomogeneous cell distribution of the scaffold. Alternatively, cell-ladened bioinks are frequently used in 3D bioprinting of cartilage tissues, providing a suitable 3D microenvironment for relevant cellular functions [30, 31]. For example, gelatin and its derivative GelMA are usually used as bioinks due to the presence of biochemical signals enhancing cell adhesion and proliferation. However, the relatively low mechanical properties, poor printability and short-term stability challenge their 3D bioprinting applications [32–34]. Methylcellulose (MC), a water-soluble cellulose derivative, has been blended with other biomaterials to enhance printability due to its high viscosity [35–37]. For example, Rastin *et al* [33] developed a range of MC (4, 6, 8 w/v%) and GelMA (5 and 10 w/v%) bioinks to enhance printability and compressive modulus (up to ∼33 kPa). Moreover, the chemically modification of MC via methacrylation to form methacrylated MC (MCMA) allows the formation of stable hydrogels with tuneable mechanical properties [38]. Due to the presence of methacrylate groups in both MCMA and GelMA, it is highly interesting to form an interconnected network (ICN) between two polymer networks, further enhancing the mechanical properties. The MCMA-GelMA ICN may result in a suitable bioink for the fabrication of a cartilage region within the OC tissue construct from the perspectives of mechanical properties and printability. However, to the best knowledge of authors, there is no reported studies using the bioink for chondrocyte encapsulation and OC tissue application, thus it is highly relevant to investigate its chondrogenic response.

This study aims to develop a simple process to fabricate a multi-cellular OC triphasic construct with a specifically incorporated calcified cartilage region for directed cell delivery and assess the suitability of MCMA/GelMA hydrogel for the cartilage region. Therefore, an integrated and extrusion-based hybrid 3D bioprinting strategy is proposed to engineer a triphasic construct, resembling the heterogeneous and zone-specific organisation and biofunctionalities of OC tissue. As shown in figure 1, PCL/TCP were firstly printed to mimic the subchondral bone region and provide sufficient mechanical support for the construct. Followed by alternative co-printing of PCL/TCP and a human adipose-derived stem cell (hADSCs) encapsulated GelMA bioink as a calcified cartilage intermediate layer. This endows the construct with a mechanical and biofunctional transition from the cartilage to the subchondral bone region, whilst also enabling *in-situ* hADSCs release to the subchondral bone layer. Finally, a human chondrocytes (HCs)-laden MCMA/GelMA bioink was used to bioprint the main cartilage zone. The ICN formation of MCMA/GelMA aims to provide sufficient mechanical strength analogous to that of native cartilage and a suitable microenvironment for HCs survival. The guided directional release and behaviour of hADSCs from the calcified cartilage intermediate layer was determined. Furthermore, HCs viability, metabolic activity, and proliferation was comprehensively assessed. Additionally, the phenotype and protein expressions of HCs at the interface and within the hydrogel matrix was investigated. This study not only fabricates a heterogeneous multilayer construct analogous to OC tissue using a novel integrated hybrid 3D bioprinting approach, but also provides engineering clues of the coordination between chondrogenesis and osteogenesis within the same construct.

2. Materials and methods

2.1. Materials

PCL (CAPA 6500, Mw = 50 kDa) was purchased from PerstorpCaprolactones (UK). TCP (Mw = 310.8 g mol^{-1}, Puriss ⩾ 98%), Dulbecco's phosphate-buffered saline (DPBS), gelatin, MC, methacrylic anhydride, sodium hydroxide (NaOH), Triton-X100, fetal bovine serum (FBS), lithium phenyl-2,4,6-trimethylbenzoylphosphinate (LAP), 10% neutral buffered formalin, and resazurin assay (Alamar blue) were obtained from Sigma Aldrich (UK). HCs isolated from normal human articular cartilage are from PromoCell (Germany). Dulbecco's modified eagle medium (DMEM), hADSCs, MesenPRO RS^{TM} basal cell culture media, phosphate-buffered saline (PBS), trypsin solution (0.25%), penicillin/streptomycin, L-glutamine, 4′,6-diamidino-2-phenylindole (DAPI), Alexa Fluor 488-conjugated phalloidin, collagen type I, collagen II, and SOX9 primary antibodies, goat anti-mouse secondary antibody Alexa Fluor 647, and Live/Dead assay kit are from Thermo Fisher Scientific (UK and Singapore). Cell counting kit 8 (CCK8) was purchased from Abcam (UK).

2.2. Synthesis of GelMA and MCMA

GelMA was synthesised using a previously reported protocol [39]. Briefly, pre-warmed DPBS was used to dissolve 10 w/v% gelatin at 50 °C, followed by the addition of 0.6 g of MA solution per 1 g of gelatin under vigorous stirring for 3 h. The solution was centrifuged at 3500 × g for 3 min to remove unreacted MA. The collected supernatant was diluted with two volumes of pre-warmed DPBS and dialysed against deionised water for 7 d at 40 °C by a dialysis membrane (12 kDa MWCO, Spectra/Por®, Fisher Scientific). The pH was adjusted to 7.4 using a 5 M NaOH solution, followed by filtration using 0.22 μm syringe filter (PES membrane, Starlab, UK) and lyophilisation by a freeze-dryer. The freeze-dried pre-polymers were stored at −20 °C and protected from light and moisture.

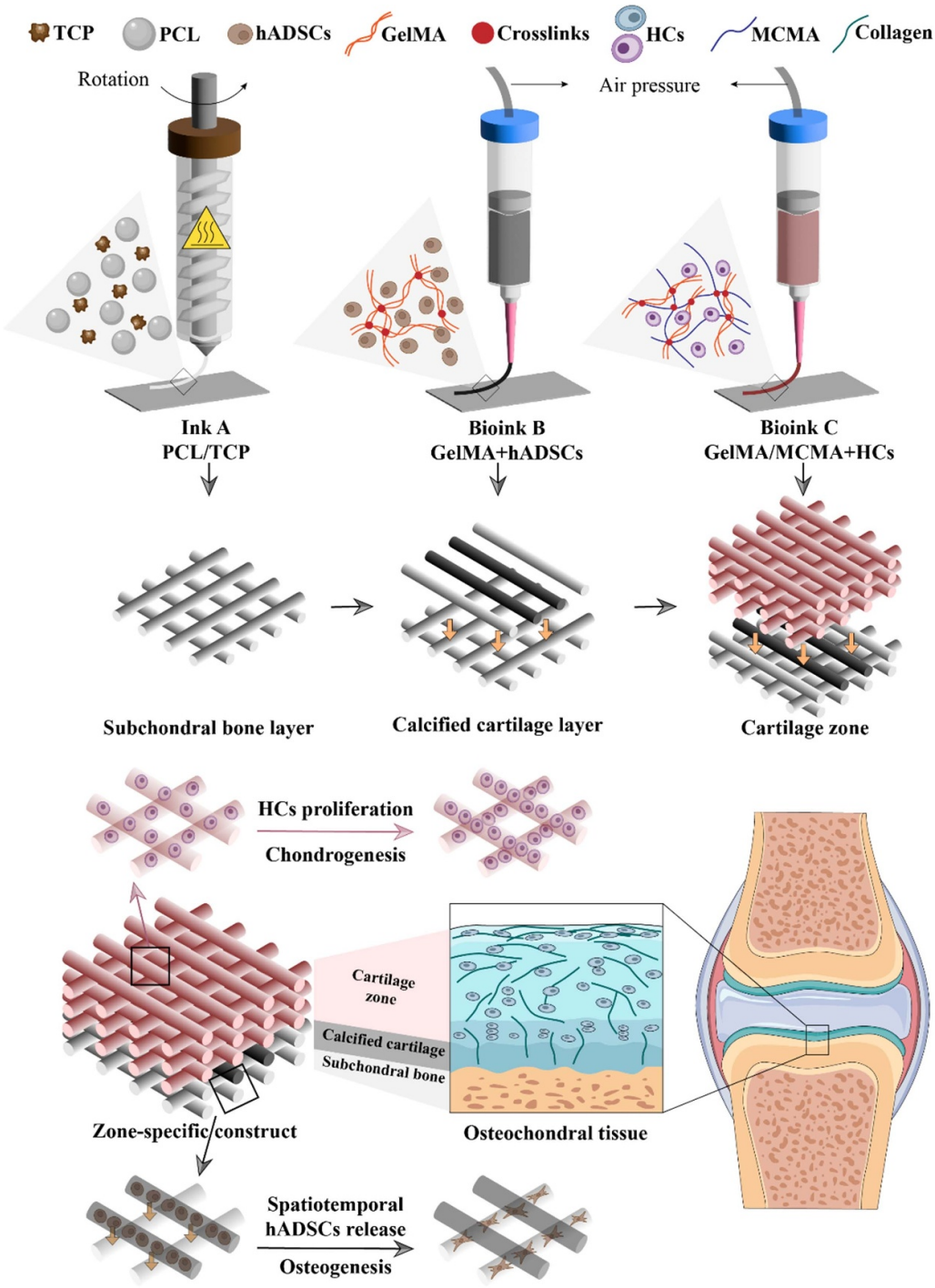

Figure 1. Schematic illustration showing the one-step hybrid 3D printing process and the design of the OC construct. The triphasic construct consists of a subchondral bone region printed using a PCL/TCP ink, a calcified cartilage layer alternatively co-printed using GelMA/hADSCs and PCL/TCP, and a cartilage region printed by using MCMA/GelMA/HCs bioink. The calcified cartilage layer allows *in-situ* release of hADSCs and attachment onto the subchondral bone layer. The interface between the calcified cartilage and cartilage layer provides a barrier function. The MCMA/GelMA bioink can maintain chondrocyte phenotype within the matrix.

To synthesise MCMA, 1 w/v% MC powder was thoroughly wetted and dissolved in 1/3 volume of DPBS at 80 °C with vigorously stirring. The remaining 2/3 volume of DPBS was subsequently added to the MC solution at 4 °C followed by further agitation for 30 min. The first addition of 2.4 ml MA per 1 g of MC was slowly added to the resulting solution allowing to proceed overnight, and an additional 1.2 mL MA was added with pH adjusted to 8.0 at 4 °C, followed by dialysis (6–8 kDa MWCO, Spectra/Por®, Fisher Scientific) at room temperature for 7 d. The solution was sterilised using 0.22 μm filters prior to lyophilisation and subsequently stored at −20 °C away from light and moisture until further use.

2.3. ^{1}H NMR

The substitution degree of methacrylation of gelatin and MC was assessed using ^{1}H NMR spectroscopy (400 MHz, Bruker, Germany). The obtained GelMA spectrum was normalised to the phenylalanine signal (6.00–7.50 ppm) representing the composition of gelatin. The integrated lysine methylene signals (2.80–2.95 ppm) were used to calculate the degree of functionalization for GelMA using equation (1). Similarly, the degree of MC methacrylation was determined by the ratio of integrals of methylene protons (6.0 and 5.6 ppm) and methyl protons (1.9 ppm) of methacrylate to carbohydrate protons according to equation (2)

$$\mathrm{DOF_{GelMA}}\,(\%) = 1 - \frac{\text{Area (lysine methylene of GelMA)}}{\text{Area (lysine methylene of gelatin)}} \tag{1}$$

$$\mathrm{DoF_{MCMA}}\,(\%) = \frac{\text{Area (methylene and methyl of MCMA)}}{\text{Area (carbohydrate of MC)}}. \tag{2}$$

2.4. Fabrication of the gradient OC construct

The PCL/TCP composite for the subchondral bone layer was prepared by heating PCL pellets to 90 °C for 20 min. Once the PCL was melted, 40 w/w% TCP powder was manually mixed with the PCL for up to 30 min ensuring a homogeneous distribution of TCP. The composite was allowed to cool and then cut into small pieces prior to use.

GelMA ink was prepared by dissolving 10 w/v% of GelMA pre-polymer in DPBS at 40 °C, followed by adding 0.25 w/v% of LAP photoinitiator. To prepare MCMA/GelMA inks, 4 w/v% MCMA (MCMA4/GelMA) or 8 w/v% MCMA (MCMA8/GelMA) was wetted and stirred in DPBS at 70 °C for 30 min and stored at 4 °C overnight, followed by dissolving 10 w/v% of GelMA and 0.25 w/v% of LAP into the solution at 40 °C. The resulting ink was centrifuged at 3500 ×g to eliminate bubbles and protected from light.

A full-thickness 3D OC construct was fabricated using a hybrid extrusion-based printing process using multi-type printheads. Two layers of PCL/TCP (subchondral bone layer) were printed in a 0°/90° lay-down pattern using a screw-assisted extrusion printhead (3D Discovery, REGENHU, Switzerland), with a 330 μm filament width, 350 μm pore size (680 μm line spacing), and 270 μm layer thickness, using a nozzle with a 330 μm inner diameter. Subsequently, PCL/TCP filaments were printed above the subchondral bone layer with a 2720 μm line spacing, followed by depositing two GelMA filaments (line space 906 μm) between each two PCL/TCP filaments using a pneumatic extrusion and temperature controlled printhead (BIOX6, Cellink, Sweden) to form the calcified layer. The main cartilage zone was fabricated by stacking 6 layers of MCMA8/GelMA in a 0°/90° lay-down pattern with a 906 μm line spacing using the pneumatic extrusion and temperature controlled printhead. The printed construct was photocrosslinked with visible light (150 s, 405 nm, 36 mW cm^{-2}, LC-L1V5, Hamamatsu, Japan), allowing the formation of stable hydrogels. The hybrid printing parameters are shown in table 1. To achieve reproducible printing of the hydrogel inks, fresh precursor solutions were prepared prior to the printing. Due to thermo-sensitivity of GelMA and MCMA, the printing temperature was kept constant. The extrusion pressure was slightly adjusted during the printing process to allow a consistent filament deposition and retain the printed filament width close to the nozzle diameter.

2.5. Rheology

A shear rate from 0.1 to 1000 s^{-1} was used to assess the changes in viscosity of the hydrogels, using the AR-G2 rheometer (TA Instruments, USA) coupled with a 20 mm diameter parallel plate. The gap size was 500 μm and the environmental temperature was set to 25 °C. A dynamic frequency scan was conducted, ranging from 0.1–100 rad s^{-1} at 1% strain, measuring both the storage modulus (G') and the loss modulus (G'').

2.6. Mechanical analysis

The photocrosslinked GelMA and MCMA/GelMA hydrogel discs ($n = 4$, height 10 mm and diameter 10 mm) were incubated in DPBS at 37 °C overnight to ensure complete swelling. The uniaxial static compression (Instron 3344 with a 10 N load cell, USA) was performed at a strain rate of 0.5 mm min^{-1} until 20% strain was achieved. For stress relaxation ($n = 3$), the strain at strain rate of 0.5 mm min^{-1} was conducted until 15% strain was achieved and held for 3000 s.

The monophasic MCMA8/GelMA (cartilage region only) and the cartilage and calcified cartilage regions of triphasic construct (cartilage-calcified-subchondral bone construct) were printed with a 906 or 2720 μm line spacing. The samples with dimensions of 5 × 5 × 10 mm ($n = 5$) were submitted to static compression. For stress relaxation ($n = 3$), the strain was increased at an interval of 2.5% at a ramp rate of 1 mm min^{-1} until 10% of strain was reached. The stress over time was recorded. The cyclic compression ($n = 3$) was conducted for 10 cycles at a rate of 1 mm min^{-1} to reach 10% of strain. The minimum recovered strain and the maximum achieved stress were analysed from the cyclic stress–stain curves.

The layer bonding strength of the triphasic construct was assessed using a rheometer (TA DHR-2 Rheometer, USA) coupled with a dynamic mechanical analyser module. Two parallel plates were 3D printed using a fused deposition modelling printer (Bambu Lab X1E, China) and clamped tightly by the upper and lower geometry mount. The samples were tightly stuck between the plates using double-side tape and glue. Two types of constructs were tested: non-interlocking triphasic structure and interlocking triphasic structure. The non-interlocking samples ($n = 4$) were fabricated following the previously mentioned OC tissue construct fabrication process. The interlocking samples ($n = 4$) were fabricated with two layers of alternatively printed PCL/TCP and GelMA filaments with a 906 μm line spacing and a 0°/90° lay-down

Table 1. Printing parameters for the hybrid fabrication process.

Material type	Screw rotational velocity (rpm)	Extrusion pressure (bar)	Speed (mm s^{-1})	Printing temperature (°C)
PCL/TCP	10	4.5	6	90
GelMA	/	1.10–1.25	6	20
MCMA/GelMA	/	1.20–1.40	6	24

pattern. The samples were tested using a rate of 10 μm s^{-1} until the delamination of the construct.

2.7. Morphology

The printed zonal construct was imaged by optical microscope (VHX-5000, Keyence, Japan). Scanning electron microscopy (SEM, TESCAN MIRA3, Czech Republic) was used to assess the microstructure of each zone. The printed samples were immersed in DPBS at 37 °C overnight, allowing full swelling of hydrogel components and subsequently lyophilised. The construct was coated by 10 nm thick layer of gold/palladium (80:20).

2.8. In vitro *studies*

2.8.1. Cell culture. hADSCs (passage 5) were cultured in MesenPRO RS^{TM} basal media supplemented with 2% (v/v) growth supplement, 1% (v/v) penicillin/streptomycin, and 1% (v/v) glutamine. The cell culture medium was refreshed every 2 d. HCs (passage 4) were cultured in high-glucose DMEM media supplemented with 10% FBS, 1% (v/v) penicillin/streptomycin, and 1% (v/v) L-glutamine.

2.8.2. hADSCs release and migration. To investigate the cell release and migration from the calcified cartilage layers, the GelMA bioink was loaded with hADSCs at a cell density of 1×10^6 cells ml^{-1}. The rest of the OC construct was acellular and fabricated using the proposed strategy. The bioprinted constructs were washed with PBS and incubated in cell culture media, and the media was changed every 2 d.

The migration was visualised using the confocal microscopy (SP8, Leica Microsystems, Germany). The sample was fixed at different time points (day 3, 7, 14, and 21) using 10% (v/v) formalin solution for 1 h and 0.2% (v/v) of Triton-X solution for 30 min to permeabilise the cell membrane. The constructs were blocked by 5% (v/v) FBS/PBS solution for 1 h, followed by the staining of 1:200 Alexa 488 phalloidin for 1 h and 1:1000 DAPI for 30 min in the dark. Cell morphology was imaged by a confocal microscope and cell area/circularity was semi-quantified using the CellProfiler software [40, 41].

2.8.3. Chondrocyte behaviour.

2.8.3.1. Cell seeding and cell encapsulation. The role of HC encapsulation and seeding was explored through two approaches. Cell encapsulated samples were either mixed with the pre-polymer bioink solutions at a cell density of 5×10^5 cells ml^{-1} and cast into a sterile acrylic mould (10 mm of diameter by 1.5 mm of height) or as a cell-laden bioink, following the previously described 3D bioprinting process. All samples were subsequently photocrosslinked for 150 s. Alternatively, for the cell seeded samples, 200 μl of cell suspension containing 5×10^5 cells was added to the surface of a 3D printed acellular hydrogel scaffold. The cells were incubated for 2 h to allow cell attachment, fresh culture medium was added to fully immerse the samples. The culture medium was refreshed every 2 d.

2.8.3.2. Cell viability. A live/dead assay was used to assess cell viability of the HCs in the hydrogels after 1, 3, 7, and 14 d of culture. The samples ($n = 4$) were stained with PBS containing 4 μm ethidium homodimer and 2 μm of calcein at 37 °C for 30 min and imaged by a confocal microscope (SP8, Leica Microsystems, Germany). Live and dead cell numbers were counted using ImageJ software. The percentage cell viability was determined by the ratio of live cells to the total cell number.

2.8.3.3. Cell metabolic activities and proliferation. Cell metabolic activity was accessed by the resazurin assay at day 1, 3, 7, and 14 of cell culture. The samples ($n = 4$) were incubated in serum-free DMEM containing 10% (v/v) resazurin solution for 4 h and the fluorescence was read (Ex/Em = 540 nm/590 nm) using a microplate reader (Spark®, TECAN, Switzerland). Cell proliferation was assessed by the CCK8 assay. Briefly, the samples were incubated in DMEM containing 10% (v/v) CCK8 solution for 4 h and the absorbance was measured at 460 nm.

2.8.3.4. Immunofluorescence analysis. Immunofluorescence staining was used to evaluate the expression of type I collagen (Col1), type II collagen (Col2), and SOX9 by the HCs at day 3, 7, 14, and 21 of cell culture. The samples were fixed with a 10% (v/v) formalin solution for 1 h, followed by permeabilisation using 0.2% (v/v) Triton X-100 in PBS for 30 min. The resulting solutions were incubated in 5% FBS solution for 1 h and incubated with either a 1:400 Col1, Col2, or SOX9 antibody solution at 4 °C overnight. Followed by Alexa Fluor 647 secondary antibody staining with a dilution of 1:100 for 1 h. Alexa Fluor 488-conjugated phalloidin with a dilution of 1:400 and a 1:1000 DAPI solution were additionally stained for 1 h and 30 min, respectively, in the dark. The samples were washed three times with pre-warmed PBS after each step and

visualised using a confocal microscope. Cell area, circularity and fluorescence intensity of Col1, Col2 and SOX9 were semi-quantified using CellProfiler software.

2.9. Statistics

Statistical analysis was conducted using one-way analysis of variance followed by Tukey multiple comparison test with GraphPad Prism (Graphpad Software Inc., USA). Significance levels were defined as $^{*}P < 0.05$, $^{**}P < 0.01$, $^{***}P < 0.001$ and $^{****}P < 0.0001$. Data are presented as mean ± standard deviation.

3. Results and discussion

3.1. Hydrogel characterisations

As the construct consists of a cartilage zone, a calcified zone and a subchondral bone zone, the biomaterial formulations are customised considering the printability and each zone' functionalities. For subchondral bone region, the superior mechanical properties and osteogenesis are the key considerations, and these have been fully demonstrated in our previous studies [29, 42, 43]. Therefore, the bioink properties specifically for cartilage zone and calcified zone are extensively investigated in this paper. To photocrosslink the hydrogel, the reactive amine and hydroxyl groups on gelatin and hydroxyl groups on MC backbone were replaced by methacryloyl groups (figure 2(a)). The degree of substitution, determined by ^{1}H NMR spectra, was 59.2% and 12.0% for GelMA and MCMA, respectively (figure 2(b)). The presence of significant peaks at 5.43 and 5.67 ppm indicates a notable increase in methacrylic vinyl groups, confirming the successful methacrylation of amino groups on gelatin. Moreover, the methyl protons of methacryloyl groups at 1.88 ppm show an increase while the lysine protons at 3.00 ppm of gelatin decrease after the synthesis. Similarly, a significant increase in methylene (6.36 and 5.91 ppm) and methyl (1.88 ppm) peaks in MCMA spectra indicates the successful conjugation of methacrylate groups onto the MC backbone.

The flow of bioinks during extrusion is driven when the applied pressure surpasses the yield stress, which may result in the encapsulated cells experiencing significant shear stress [44]. In this case, the ability of the bioinks to exhibit shear-thinning behaviour is critical as it enables the bioink to flow at low pressures, reducing cell damage. Figure 2(c) shows that the developed hydrogels display a shear-thinning behaviour, exhibiting a decreased viscosity with the increase of shear rate. This is due to the disentanglement of polymer chains at an increased shear rate, leading to a decreased viscosity. In addition, higher viscosity of MCMA/GelMA is observed by increasing the concentration of MCMA. The storage modulus G' represents the material shape retention ability, indicating its gel strength, while the loss modulus G'' reflects its ability to dissipate energy [44]. As shown in figure 2(d), the GelMA and MCMA/GelMAs show frequency-dependent behaviour, and a higher storage modulus than loss modulus ($G' > G''$) is observed, indicating a dominant effect of a viscoelastic solid-like behaviour. Additionally, the storage modulus was significantly enhanced by increasing the MCMA concentration, indicating an improved mechanical strength and better shape retention ability compared to GelMA.

As observed in figure 2(e), the compressive modulus of the photocrosslinked hydrogels ranges between 48 and 516 kPa. GelMA presents the lowest compressive modulus (∼48.16 kPa), and the modulus significantly increases by increasing the concentration of MCMA (∼219.79 kPa for MCMA4/GelMA and ∼516.33 kPa for MCMA8/GelMA). Studies indicate that the compressive modulus of human articular cartilage typically is between 240 to 1000 kPa [45–47], and MCMA8/GelMA falls within this range. This can be attributed to the ICN formation through the establishment of covalent bonds between GelMA and MCMA. Additionally, compared to GelMA, the MCMA/GelMA shows a faster stress relaxation, which is strongly associated with the cell spreading and migration within the hydrogel matrix [48] (figure 2(f)). This might be due to the reversible physical hydrophobic associations within the MCMA polymer network providing dynamic crosslinking sites, which dissipate stresses.

3.2. Hybrid printing of zonal-specific OC construct

Native OC tissue presents an approximate thickness of 3 mm [1], with the articular cartilage region ∼ 2–2.34 mm [49, 50], the subchondral bone ∼ 0.52 mm [51], and the thin calcified cartilage interface layer ∼5% of the total OC thickness [1]. Therefore, the zonal-specific OC construct was designed and fabricated according to these dimensions (figures 3(a)–(d)). Two subchondral bone layers (0.33 mm of layer thickness) were firstly fabricated by melt-extrusion printing PCL/TCP layers mimicking the subchondral bone region and providing mechanical support. The use of PCL incorporated with a high concentration (40 w/w%) of TCP particles was based on our previous results which demonstrated the enhanced osteogenic differentiation of hADSCs and mechanical properties [29]. In particular, the PCL/TCP scaffold has ∼7 MPa compressive modulus aligning with the range of the native subchondral bone modulus (10–3000 MPa) [52–54]. The optimised printing parameters (screw velocity, printing speed, pressure, and temperature) were determined by measuring the printed filament width and aiming to match the nozzle diameter. A single layer was then fabricated by alternatively printing PCL/TCP filaments and GelMA filaments, mimicking the calcified layer. In this layer (0.33 mm of layer thickness), PCL/TCP filaments were used to provide mechanical support for the soft GelMA structure and to improve adjacent phase bonding with the subchondral bone layer. The co-printing pattern improves the integration between subchondral bone and cartilage region, creating a transition layer with gradually changing mechanical properties from the hard to the soft interface. Moreover, the GelMA filaments will be loaded with hADSCs and aim to release the cells *in-situ* onto the subchondral bone layer

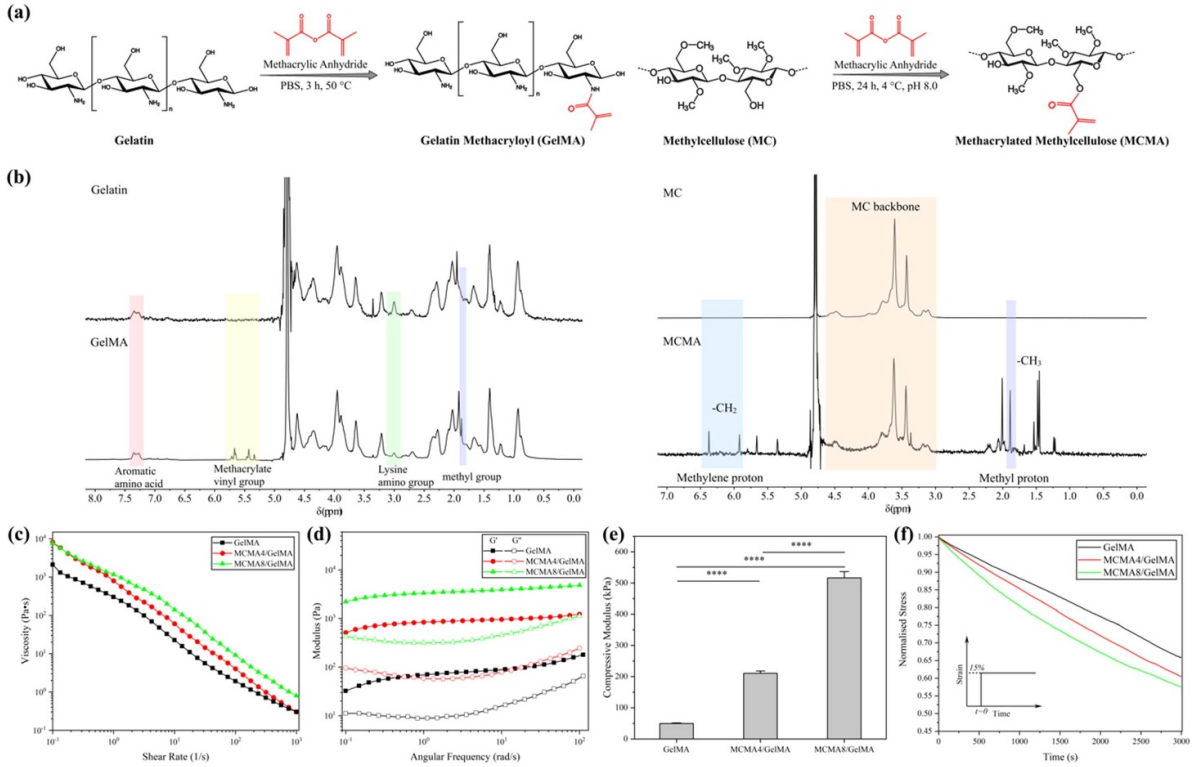

Figure 2. Hydrogel characterisations showing (a) chemical modifications of gelatin and MC by methacryloyl groups. (b) ^{1}H NMR spectra of GelMA and MCMA confirming the successful methacrylation of gelatin and MC. (c) Shear rate sweep showing shear-thinning behaviour of inks. (d) Frequency sweep showing the storage modulus G' and loss modulus G'' against the angular frequency for all inks. (e) Compressive modulus of all hydrogel discs. (f) The stress relaxation behaviour of all hydrogel discs.

through cell migration and attachment. It is reported that high stiffness hydrogels are potentially suitable for cartilage applications [55–57]. Considering the higher gel strength of MCMA8/GelMA and to mimic the cartilage region, six layers of MCMA8/GelMA (0.26 mm of layer thickness) were printed on top of the calcified layer, followed by photocrosslinking to achieve stable hydrogel layers.

The hybrid extrusion bioprinting endows the construct/scaffold with heterogeneity by selectively and regionally depositing different cell populations and materials. It can be observed in figures 3(a)–(d) and supplementary Video S1 that each region of the OC construct was printed with high precision and exhibited a distinct zonal structure as designed. The 3D porous PCL/TCP layer zone exhibits a well-defined structure with uniform circular cross-sections and a smooth surface, indicating a stable printing process (figure 3(e)). The measured PCL/TCP and GelMA filament diameter and pore size are closely aligned with the designed parameters (table S1). The high magnification SEM figure shows the homogeneously distributed TCP particles at the surface of the filament. As a transition interface layer, GelMA filaments were successfully printed between PCL/TCP filaments without collapse (figures 3(a)–(c)). In addition, the developed MCMA/GelMA ink presented good printability and supported multiple layer printing without requiring a layer-by-layer photocrosslinking process. The printed cartilage layer presents an orderly arranged structure with interconnected macroscopic pores and structural stability. Moreover, a uniform lattice network structure of the printed MCMA/GelMA layers is observed with a dense microporous internal structure (figure 3(e)). A slightly increased filament diameter and decreased pore size is observed compared to the designed parameters, this is mainly attributed to the hydrogel swelling (table S1). Compared to the soft hydrogels, the highly viscous PCL/TCP composite can be stably printed. The screw-assisted extrusion printing facilitates smooth and stable flow of the high concentration PCL/TCP composite. In contrast, the printability of GelMA and MCMA/GelMA is strongly associated with their concentration, environmental factors (e.g. temperature), and even storage conditions (e.g. storage time and temperature). For a reproducible hydrogel printing, a freshly prepared bioink is required since long-term storage of GelMA and MCMA/GelMA prepolymer may suffer from hydrolytic degradation and a decrease in viscosity, thus changing the printing parameters. Additionally, both GelMA and MCMA/GelMA are temperature-sensitive hydrogels. The sol–gel transition of GelMA derives from the polypeptide chain entanglement at low temperatures [58–60], whereas the gel formation of MCMA above the lower critical solution temperature is because of the hydrophobic association and self-assembly processes [61, 62]. The printing temperature was therefore strictly controlled by the temperature-controlled

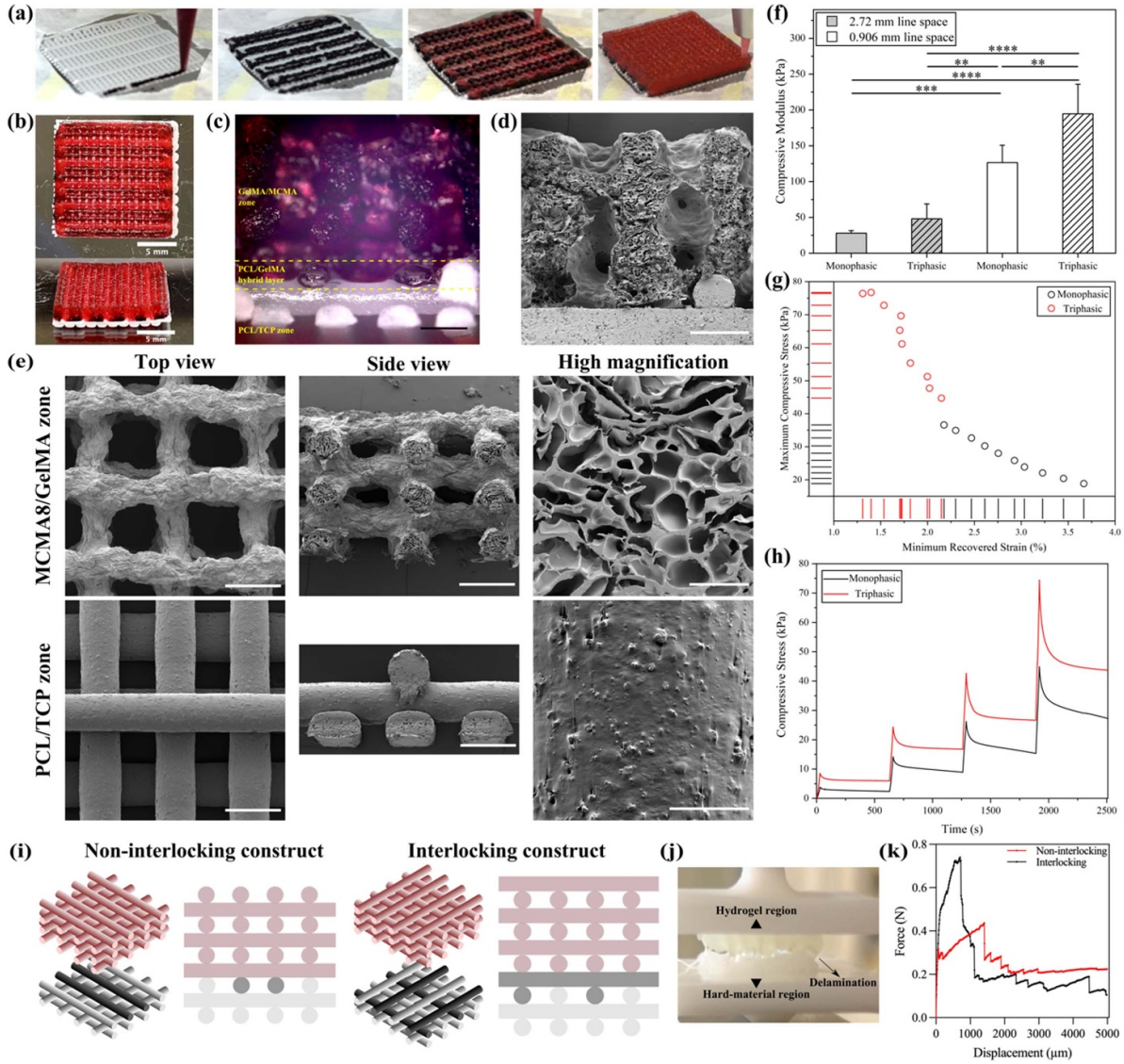

Figure 3. Physical properties of zonal-specific OC construct. (a) Hybrid printing process and (b) top and side view of the printed triphasic construct. To aid visualisation the GelMA and MCMA8/GelMA ink are stained with black and red dye, respectively. (c) Microscope image and (d) SEM image showing the cross-section of the triphasic construct with a distinct zonal structure. (Scale bar: 500 μm). (e) Hydrogel SEM images showing top, side, and high magnification views of MCMA8/GelMA layer and PCL/TCP layer. (Scale bar: top and side view, 500 μm; MCMA8/GelMA high magnification, 50 μm; PCL/TCP high magnification, 100 μm). (f) Compressive modulus of the printed monophasic and triphasic construct with variable line spaces. (g) Minimum recovered strain and maximum stress from cyclic compression curves and (h) stress relaxation profiles for triphasic and monophasic constructs. (i) Schematic showing non-interlocking and interlocking constructs. The non-interlocking construct has a single calcified cartilage layer with a double line of GelMA filaments and a single PCL/TCP filament. For the interlocking construct, two calcified cartilage layers are printed with alternative co-printing of PCL/TCP and GelMA filaments (light grey filament: PCL/TCP; dark grey filament: GelMA; red filament: MCMA8/GelMA). (j) Image showing the delamination of layers at the soft hydrogel and hard material interface. (k) Force-displacement profiles showing the delamination process of non-interlocking and interlocking construct.

printhead in this work, avoiding any printing distortion. Nevertheless, despite maintaining a constant printing temperature and speed, the printing pressure was continuously monitored to ensure optimal extrusion, with subtle adjustments to account for any changes in the hydrogel status (e.g. the friction between hydrogel and chamber wall and water content).

The mechanical properties of the triphasic and monophasic constructs were assessed by static and dynamic compression as well as stress relaxation. The triphasic construct refers to the developed hybrid zonal OC construct and the monophasic cartilage-only region construct (MCMA8/GelMA scaffold) is used as a reference. Figure 3(f) shows the compressive modulus of both monophasic and triphasic constructs printed with different filament line spacing. The triphasic construct has a significantly higher compressive modulus than that of the monophasic construct due to the presence of the

reinforced PCL/TCP layers. Moreover, the construct with a smaller line space (0.906 mm) presents significantly higher compressive modulus than that with a larger line spacing, and the modulus of the triphasic construct reaches approximately 190 kPa. Compared with the compressive modulus of the casted hydrogels (i.e. MCMA8/GelMA) and melt extruded PCL/TCP, the overall compressive modulus of the triphasic construct is lower due to the use of a porous hydrogel structure. Furthermore, the hydrogels represent the majority of the triphasic construct and with a loading of 20% strain, the cartilage region (MCMA8/GelMA) deforms predominately. However, by altering the structural design, the compressive modulus can be significantly enhanced, for example, utilising a core-shell strategy for the cartilage region (figure S1). A PCL shell is used to envelope a 100% infill MCMA8/GelMA core (cartilage region), transferring the load to the PCL and restricting the deformation of the hydrogel. Alternatively, electrowriting of embedded PCL microfibres has been demonstrated to reinforce hydrogel constructs [63]. Additionally, modulating the hydrogel concentration and crosslinking density [64], or the utilisation of freeze-casting and salting-out approaches can improve the mechanical properties [65]. The dynamic compression results in figure 3(g) show the maximum compressive stress reached at 10% strain against the minimum recovered strain (when 0 MPa of stress is reached) for each cycle. It can be observed that the triphasic construct shows higher maximum compressive stresses at 10% of strain and lower minimum recovered strains when the stress is removed, suggesting a stronger mechanical strength and better recoverability after the deformation compared to the monophasic construct (figure S2). In addition, both constructs display stress relaxation behaviours with the stress decreasing over time at each strain-holding phase (figure 3(h)). The monophasic construct presents slower stress relaxation compared to the triphasic construct, with the triphasic construct reaching the equilibrium state within a shorter relaxation time. This may be due to the subchondral bone layer and calcified layer dissipating the stress under force within their interconnected porous structure.

To investigate the bonding strength between different zones, the triphasic construct with and without mechanical interlocking layers were fabricated and the delamination force was assessed (figures 3(i)–(k)). Attributed to similar material formulation and crosslinking strategy, the GelMA fibres and MCMA/GelMA fibres present a strong bonding, leading to a good integration at the interface between the hydrogel components of the calcified cartilage and cartilage layers. The delamination between the layers mainly occurs at the soft hydrogel and hard material interface i.e. between GelMA or MCMA/GelMA and PCL/TCP (figure 3(j)). The results show that the interlocking construct has a higher maximum separation force ($\sim$0.73 N) compared to the non-interlocking construct ($\sim$0.42 N), indicating an enhanced interfacial bonding strength (figure 3(k) and table S2). The bonding strength relies on the gel strength of GelMA under bending and can be further increased by increasing the number of GelMA fibres and interlocking layer. Nevertheless, despite the poorer bonding efficiency, for the purpose of better illustrating the cell release process and simplifying the manufacturing process, the non-interlocking design was used for the rest of the study.

3.3. Biofunctionality of the calcified layer and cartilage layer

3.3.1. hADSCs release from the calcified cartilage layer.

The subchondral layer was fabricated using PCL/TCP, our previous studies demonstrate its biocompatibility and ability to support osteogenesis [29, 42]. Therefore, in this study, only the biofunctionality of the calcified cartilage layer and the cartilage layer were investigated. One of the aims of the calcified cartilage layer is to be able to release hADSCs, allowing the cells to migrate to the stiffer PCL/TCP subchondral bone zone rather than to the softer MCMA/GelMA cartilage layer. To mimic the cell release process, the triphasic construct was fabricated and hADSCs were encapsulated in the GelMA filaments, while the rest of layers were acellular.

Confocal cross-sectional images presented in figures 4(a)–(c) show both cell distribution and morphology in the construct. The cells at the bone-calcified cartilage (PCL/TCP-GelMA) and cartilage-calcified cartilage (MCMA8/GelMA-GelMA) interfaces were investigated. It can be observed the rounded morphology of hADSCs at both interfaces at day 3, indicating the 3D confinement effect of the hydrogel matrix on cells. The presence of hADSCs in the acellular MCMA8/GelMA is due to the slight merging between adjacent GelMA and MCMA8/GelMA layers (figure 4(a)). However, cells in the GelMA matrix show a larger cell area and a lower cell circularity compared to those in the MCMA8/GelMA matrix due to the larger pores and lower stiffness of GelMA (figures 4(b) and (c)). Moreover, after 14 d, the hADSCs still present rounded cell morphology in the MCMA8/GelMA matrix with significantly lower cell area and higher circularity and few spread cells were detected far from the cartilage-calcified cartilage interface, indicating their 'quiescence' state and low cellular activities in the dense and stiff hydrogel system [66]. These results indicate that the MCMA8/GelMA with a dense internal porous structure successfully restricts cell migration upwards from the calcified layer, mimicking the native biofunctions of the cartilage zone. Contrastingly, it can be observed that cells are released from the GelMA matrix and attach to the PCL/TCP layer at day 14, indicating successful cell release and migration (figure 4(a)). Moreover, cells exhibit a spread and elongated morphology along the direction of the printed filament, with a significantly decreased cell circularity and increased cell area. A good anchoring and stretched morphology of hADSCs on the PCL/TCP filaments (figure 4(d)), and a highly spread cell cytoskeleton in the GelMA matrix (figure 4(e)) suggest that the triphasic construct is capable to support cell release and migration spatiotemporally from a softer 3D hydrogel matrix to the stiffer 3D thermoplastic substrate, allowing the regular cell functions of hADSCs such as attachment and proliferation.

The interplay between cells and the ECM matrix, especially in a 3D microenvironment, are complex. For example,

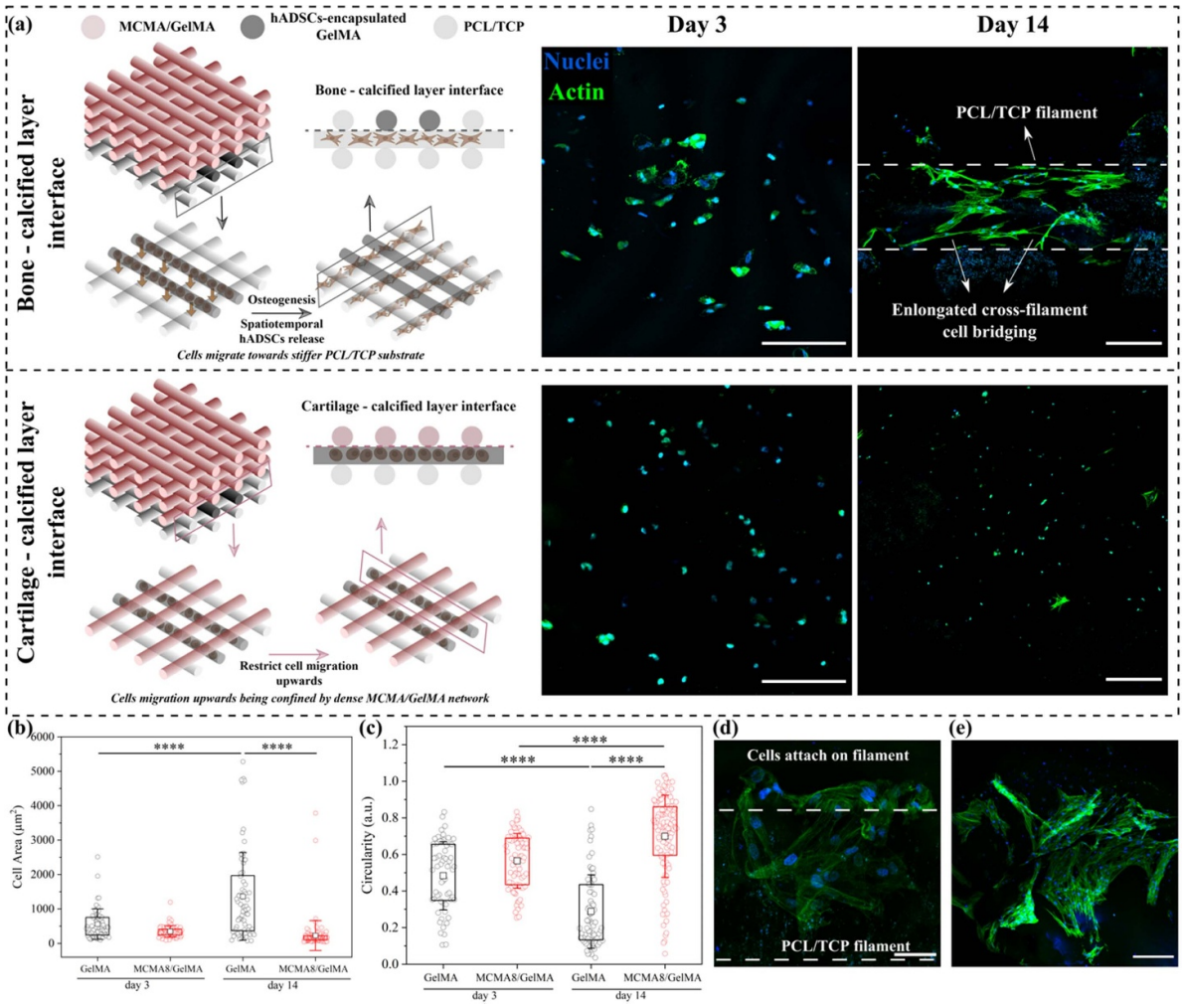

Figure 4. hADSCs released from the calcified layer and their migration process at the interfaces. (a) Schematic illustrations showing the guided cell migration at the bone-calcified interface (top) and restricted cell mobility at the cartilage-calcified interface (bottom) and their representative confocal images showing cell morphology and migration process after 3 and 14 d of culture (scale bar: day 3, 100 μm; day 14, 200 μm). At the bone-calcified interface, cells migrate towards to the stiffer PCL/TCP substate while cell movement from calcified layer upward to cartilage region is restricted and confined due to denser MCMA/GelMA matrix and gravity. Red filaments represent MCMA8/GelMA; dark grey filaments represent GelMA encapsulated with hADSCs, and light grey filament represents PCL/TCP fibres. (b) Semi-quantification of cell area and (c) cell circularity. (d) Confocal image showing cell clusters anchoring on the PCL/TCP filament at day 14 (scale bar: 50 μm) and (e) cell spreading in the GelMA matrix (scale bar: 200 μm).

rheological behaviour of bioinks might be affected by the encapsulated cell due to the physical constraints of polymer chains, thus leading to a limited structural stability and a potential layer merging before photocrosslinking [67, 68]. The merging did occur at the calcified cartilage-cartilage interface. Although it is conducive to the smooth transition of two distinct layers, enhancing the integration of the whole construct. There is a potential risk of allowing blood, bone, and immune cells to penetrate into the articular cartilage region during and after implantation. Alternatively, cell migration requires the cell to remodel the dense ECM micropores and perform relevant cell functions. These involve a variety of factors, including the composition of ECM, stiffness, crosslinking, pore size, ECM remodelling capacity, and gravity [69, 70].

In this study, the sandwich structural design allows hADSCs moving from the intermediate calcified cartilage GelMA layer downwards to the PCL/TCP layer guided by material design and gravity [71]. Moreover, hADSCs can easily pass through the larger micropores of GelMA and migrate towards to the subchondral bone layer. The significantly distinct differences in stiffness between GelMA matrix and PCL/TCP layer may guide cell migration in the form of durotaxis towards the higher stiffness thermoplastic substrate [72, 73]. Durotaxis is the process by which cells migrate in response to ECM stiffness gradients, moving to preferred substrates [74]. The hADSCs sense the PCL/TCP stiffness by deforming their surroundings through forces they generate and move towards the

substrate. Additionally, the rough surface of the PCL/TCP substrate supports cell adhesion and osteogenesis [29]. The presence of TCP provides bioactive calcium and phosphate ions, acting as chemotactic signals and attracting cells to the region [75].

Conversely, the migration of hADSCs to the MCMA8/GelMA matrix is restrained due to the specific biophysical and biochemical properties of MCMA8/GelMA matrix. The MCMA8/GelMA hydrogel has a higher stiffness and crosslinking density compared to GelMA matrix, resulting in a denser and more restrictive microenvironment. Moreover, cell migration is strongly dependent on the cell ability to interact with and remodel the surrounding ECM in a 3D matrix. There is an upper limit to the stiffness of 3D matrix that allows cells to gather adhesive ligands and remodel the matrix [76, 77]. The stiffness of MCMA8/GelMA matrix may exceed this limit, leading to the decreased integrin bindings. Without sufficient adhesive ligands, hADSCs cannot establish cellular tension, resulting in limited cell migration and a more circular cell morphology. The *in-situ* hADSCs release strategy in this study leverages a series of physicochemical and structural cues, allowing a precise directional deliver of hADSCs and retaining cellular composition and functionality of each region.

3.3.2. Chondrocyte behaviour in bioinks. It is critical to evaluate the HCs behaviour in response to the bioink formulations and without the influence of extrusion-based bioprinting. Photocrosslinked casted HC-encapsulated hydrogel samples were assessed for their cell viability, metabolic activity, and proliferation figures 5(a) and (b) show the cell viability after 1, 3, 7, and 14 d of culture. It can be observed that HCs are evenly distributed in the hydrogel matrix without noticeable cell clusters. At early culture time, all samples present high cell viability (>90%), and MCMA/GelMAs show higher cell viability than GelMA group at day 1 but no statistical difference is observed at day 3. At later culture times (day 7 and day 14), the GelMA group shows significantly decreased cell viability (>80%), while higher cell viability (>90%) is observed in the stiffer MCMA/GelMA hydrogels. Interestingly, MCMA4/GelMA exhibits the highest cell viability at day 7, however after 14 d of cell culture, MCMA8/GelMA shows significantly higher cell viability than the other two groups. These results indicate that all the developed bioinks are cytocompatible at both early and later culture stages, and a stiffer MCMA/GelMA environment may be more favourable for HCs viability.

Cell metabolic results show an increasing trend with cell culture time for all hydrogels, suggesting an increased cell growth (figure 5(c)). No significant differences in cell metabolic activity at early culture times (day 1 and day 3) were observed between groups. However, MCMA4/GelMA presents a significantly higher value than the GelMA group at day 7. At day 14, both MCMA/GelMA groups exhibit significantly increased values in fluorescence intensity than GelMA, indicating that the MCMA/GelMA bioink enhances cell metabolic activity of HCs at a long-term culture period. Moreover, this observation is corroborated with the proliferation results (figure 5(d)). MCMA/GelMAs show an increased trend of absorbance value over 14 d, indicating an increase in cell number. Additionally, MCMA8/GelMA presents a notably higher absorbance value than GelMA at day 14, suggesting an enhanced cell proliferation. No statistical differences were observed between groups at the early culture stage.

3.3.3. Chondrocyte phenotype at the interface and within bioink matrix. To further evaluate the HC behaviour in the photocrosslinked casted hydrogel samples the expression of the chondrogenic marker, Col2, was assessed at the liquid-matrix interface and within the bulk matrix. Figure 6 shows the confocal images obtained from the surface of the hydrogels. The results show that after 3 d of culture, Col2 is mainly expressed at the nucleus (figures 6(a) and S3). A significantly higher Col2 expression can be observed in the MCMA/GelMAs, showing a significantly higher fluorescence intensity per cell than that of GelMA at both early and late culture stages (figure 6(b)). Interestingly, MCMA4/GelMA presents the highest expression of Col2 at day 3 among all groups. Moreover, by increasing the culture time, MCMA8/GelMA shows a notably higher Col2 expression than those of MCMA4/GelMA and GelMA at days 14 and 21 and Col2 expression at cytoplasm is observed.

Two distinct cell morphologies are observed at the hydrogel surface interface over 21 d of cell culture. Most HCs present a typical rounded morphology in the GelMA group at day 3, while the cytoskeleton of HCs start to spread in the MCMA/GelMA groups. Semi-quantification of cell circularity shows that the GelMA group exhibits a significantly higher circularity value and lower cell area at day 3 (figures 6(c) and (d)). After 7 d of cell culture, HCs in GelMA remain rounded, while most of the HCs in MCMA/GelMA samples show a notably decreased circularity and increased cell area. An elongated and spread cell morphology is observed in the GelMA at late culture time (days 14 and 21). In contrast, within the bulk of the hydrogel matrix, HCs maintain a consistent rounded cytoskeleton morphology for all samples throughout 21 d of culture (figure S4). 3D reconstructed confocal images further demonstrate these distinct cell morphologies, where a monolayer of HCs spreading over the 2D matrix surface is observed, while a rounded morphology is maintained within the 3D hydrogel matrix (figure S4).

Interestingly, HCs at hydrogel surfaces exhibit a more spindle-like cell morphology similar to precursor osteogenic cells (e.g. pre-osteoblasts), suggesting a potential transdifferentiation of chondrocytes to an osteoblast-like lineage, which may contribute to osteogenesis at the interface of these hydrogels [78]. This highlights the importance of engineering the microenvironment and positioning of surface interfaces to direct specific differentiation in the appropriate location i.e. the calcified cartilage or subchondral bone

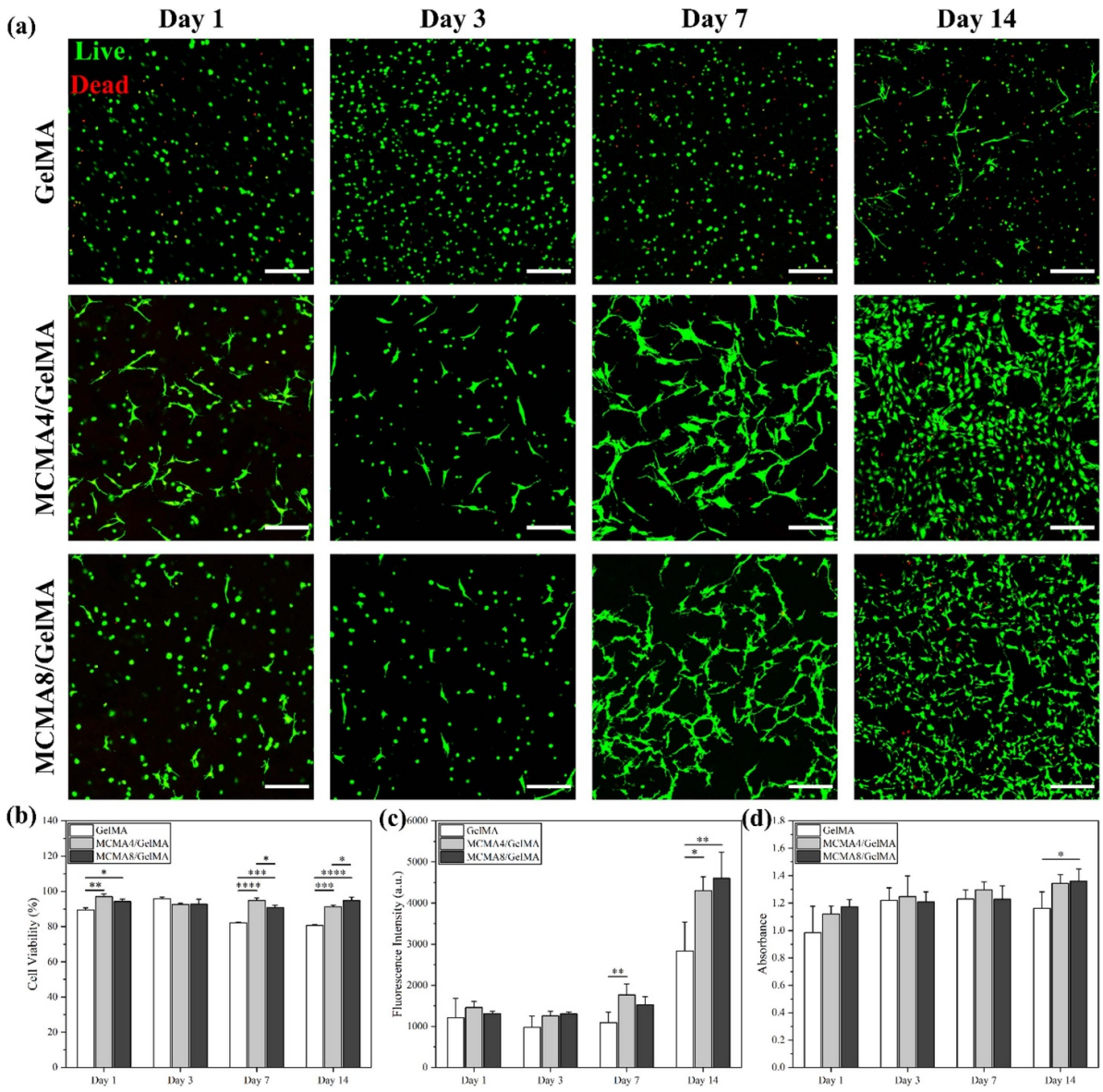

Figure 5. HC behaviour at the liquid-matrix interface in photocrosslinked casted hydrogels. (a) Representative confocal microscopy images showing live and dead results of HCs at days 1, 3, 7, and 14 (scale bar: 200 μm; green = live and red = dead). (b) Percentage cell viability. (c) Cell metabolic activity and (d) proliferation results over 14 d of cell culture.

regions enabling the seamless integration of the entire construct. During bone growth and remodelling, bone can be formed through cartilage to bone conversion via endochondral ossification [79]. In this process, hypertrophic chondrocytes can directly differentiate into osteoblasts [80]. Therefore, there might be a temporary co-expression of markers (e.g. Col2) associated with both chondrocytes and osteoblasts as cells transit from one phenotype to another.

To further understand the HCs phenotype and potential trans-differentiation due to the change in the surrounding microenvironment, i.e. at the liquid-matrix interface or within the matrix, HCs were either seeded on the printed sample surface or encapsulated within the bioprinted sample. The expression of osteogenic marker Col1, chondrogenic markers Col2 and SOX9 were analysed after 21 d of culture. As shown in figure 7(a), the seeded HCs attached to the liquid-matrix interface present a spread and elongated morphology, while encapsulated HCs maintain a round morphology in both GelMA and MCMA8/GelMA. All samples display a co-expression of Col1, Col2, and SOX9 (figures 7(b)–(d)). In GelMA samples, the encapsulated HCs show significantly higher expression of Col1 and SOX9 compared to the seeded samples, while the Col2 expression remains a similar level. Despite maintaining a rounded cell morphology in the GelMA matrix, both markers of osteogenesis and chondrogenesis increase. However, the encapsulated HCs in MCMA8/GelMA exhibit a lower expression of Col1 but significantly higher Col2 and SOX9, indicating that chondrogenesis is well maintained within the

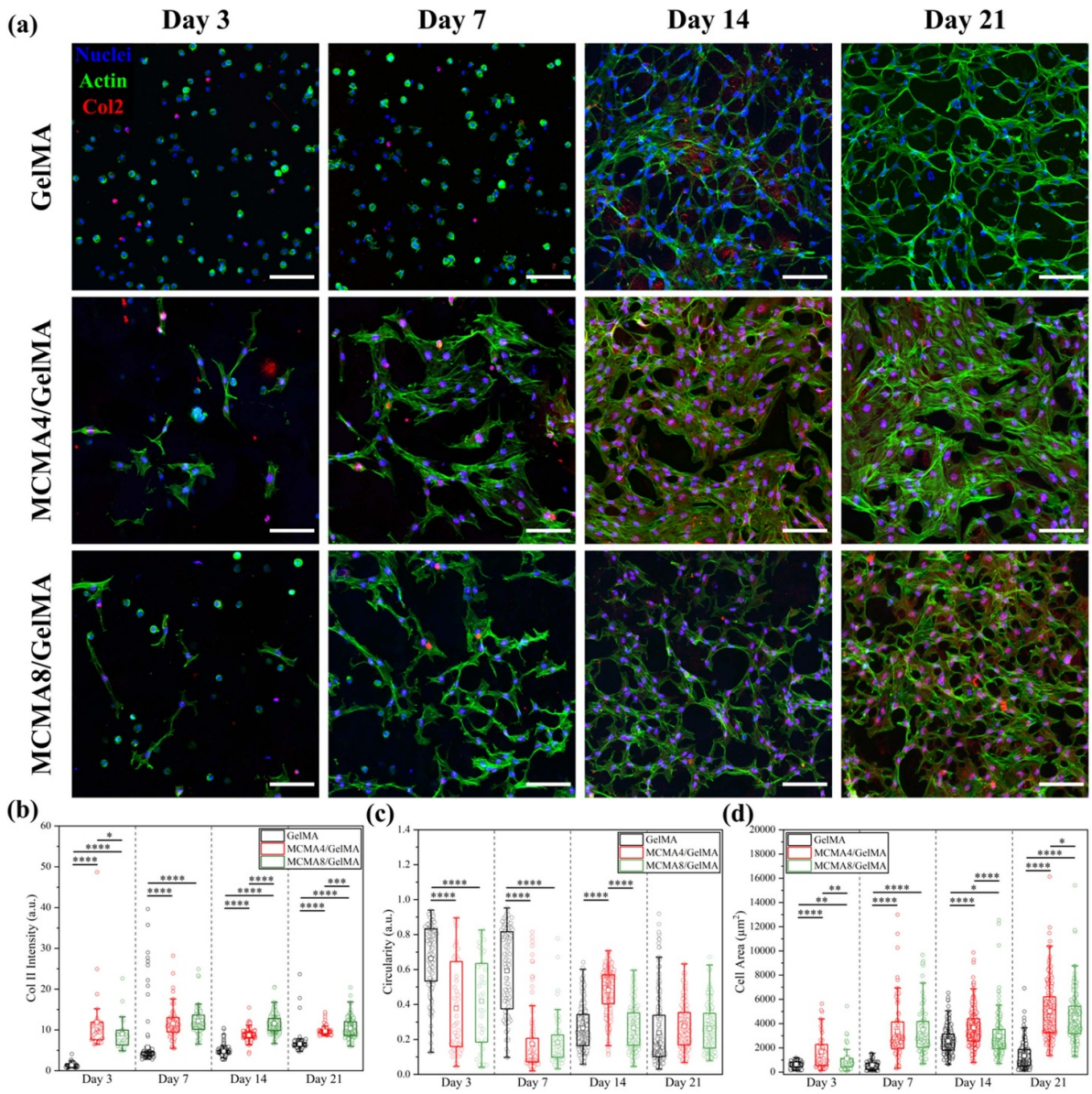

Figure 6. Encapsulated HCs at the liquid-matrix interface of the photocrosslinked and casted hydrogels. (a) Immunofluorescence images showing nucleus (blue), actin (green) and Col2 expression (red) for all samples at days 3, 7, 14, and 21 (scale bar: 100 μm). (b) Semi-quantification of Col2 expression intensity. Cell morphology analysis showing (c) cell circularity and (d) cell area.

MCMA8/GelMA matrix. These results demonstrate that HCs are more likely to maintain a chondrogenic phenotype within the hydrogel matrix, particularly in the MCMA8/GelMA matrix, while they display a trend of trans-differentiation potentially into an osteogenic lineage at the hydrogel liquid-matrix interface.

Stress relaxation is a critical factor in regulating cell behaviour. The limited stress relaxation in GelMA indicates that the matrix maintains the initial stiffness, while the MCMA/GelMA can relax the forces through matrix reorganisation, conducive to ligand clustering and cell spreading (figure 2(f)). At the late culture stage, the significantly increased metabolic activities and proliferation of HCs in MCMA8/GelMA are aligned with its faster stress relaxation characteristics as well as the level of Col2 and SOX9 deposition. These results can be correlated to a study by Lee *et al* [81], which demonstrated that the impact of matrix stiffness on cartilage matrix formation is diminished in hydrogels with faster relaxation. Furthermore, Huang *et al* [82] linked the dynamic mechanical properties of the hydrogel with cytoskeletal changes during chondrogenesis and found that slow stress relaxing hydrogels lead to the Rho-associated kinase (ROCK) dependent cell apoptosis while the faster relaxing hydrogels, acting as ROCK inhibitors, mitigate the myosin hyperactivation and cell apoptosis, promoting the long-term chondrogenesis of MSCs.

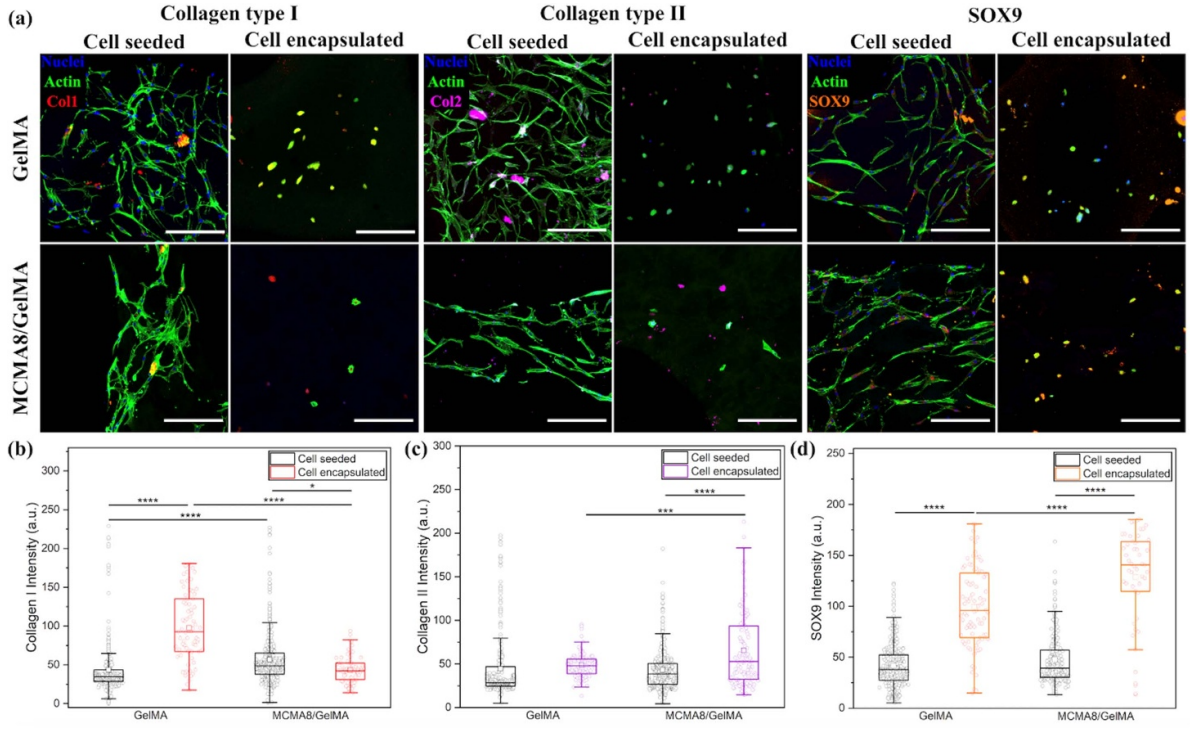

Figure 7. The seeded HCs at the liquid-matrix interface of the printed construct and encapsulated HCs within the bioprinted construct. (a) Immunofluorescence images showing nuclei (blue), actin (green), and expression of osteogenic marker Col1 (red), and chondrogenic markers Col2 (purple), and SOX9 (orange) for all samples at day 21 (scale bar: 200 μm). Analysed expression intensity of (b) Col1, (c) Col2, and (d) SOX9 for all samples.

The spreading HC morphology and potential chondrocyte-to-osteoblast trans-differentiation mainly occurs at the surface of the hydrogels, similar to a 2D *in-vitro* culture scenario. The encapsulated HCs within the hydrogel matrix better recapitulate those of a 3D native microenvironment and exhibit significantly higher chondrogenic production of Col2 and SOX9. Unlike the cells on the surface of the hydrogel, HCs within the hydrogel matrix experience isotropic matrix interactions and constraints and minimal environmental influences. These properties are crucial for the matrix to resist gravity-driven downward migration of HCs. Despite a rounded cell morphology observed in the cell encapsulated GelMA sample, a higher level of Col1 is expressed. However, in the MCMA8/GelMA matrix, HCs maintain a low Col1 expression but higher levels of Col2 and SOX9 expression. This might be attributed to the denser and highly crosslinked MCMA8/GelMA matrix providing a hypoxic microenvironment highly analogous to articular cartilage which has a low oxygen tension (1%–3%) [83]. The hypoxic environment drives cartilage matrix accumulation and downregulates degrading enzymes and hypertrophic markers to maintain a chondrocyte phenotype [83–85]. Moreover, SOX9 plays a key role in regulating osteogenesis by inhibiting the expression of Runt-related transcription factor 2 and Osterix [86]. High expression of SOX9 suggests the maintenance of a chondrogenic phenotype. These results demonstrate that the developed MCMA/GelMA bioink is potentially suitable for the constitution of the cartilage zone. Moreover, the chondrogenic-to-osteogenic trans-differentiation observed on the MCMA/GelMA surface could be utilised to engineer a gradual transition from the cartilage to bone phase.

4. Conclusions

In this study, an OC construct integrating multi-material and multi-cellular bioinks that mimics the hierarchical structure of the native tissue has been developed. The construct leverages the advantages of extrusion-based multi-printhead 3D bioprinting to fabricate heterogeneous OC construct consisting of a subchondral bone, calcified cartilage, and cartilage region. The fabricated construct demonstrates the high precision of the printing processes and the ability to withstand static and dynamic compressive loadings. The calcified cartilage layer co-printed with a cell-laden GelMA and PCL/TCP, establishes a transitional barrier between the cartilage and the subchondral bone layer. Furthermore, the directional *in-situ* release of hADSCs from the GelMA towards the acellular PCL/TCP subchondral bone layer was demonstrated. The MCMA/GelMA bioink used to fabricate the cartilage layer improves biocompatibility through enhanced cell viability, proliferation, and higher expression of key chondrogenic markers, Col2 and SOX9. The HCs tend to maintain a chondrocyte phenotype within the 3D hydrogel matrix, while a loss

of chondrogenic phenotype and potential chondrogenic-to-osteogenic trans-differentiation, recognised by co-expression of Col1, was observed at the liquid-matrix hydrogel interface. Overall, this functional construct provides a potential strategy for OC tissue engineering.

5. Future perspectives

The future of the 3D bioprinted OC construct developed in this study is promising due to several key advancements and innovations. For example, the development of advanced bioinks that better replicate the complex biomechanical and biochemical environment within OC tissue such as the cartilage mimicking stress relaxation profile and stiffness of MCMA/GelMA. Furthermore, the novel construct, integrating tailored bioinks and biomaterial inks for each zone of the OC tissue, allows the precise encapsulation of different cell types, enabling the induction of regional osteogenesis and chondrogenesis. Nevertheless, the current OC construct exhibits distinct material phases representing the different regions of the tissue. This could be improved by incorporating a continuous gradient in material properties such as a gradual reduction in TCP concentration from the subchondral bone to the calcified cartilage or varying the ratio of MCMA/GelMA mimicking the different regions within cartilage (e.g. deep, middle, and superficial zones). Additionally, elucidating the differing cell response at the interface or within the hydrogel matrix facilitates the further design of the functional graded and integrated OC construct. Furthermore, the design of the cartilage specific bioink could be improved by the addition of biomolecules such as hyaluronic acid and specific growth factors (e.g. TGF-β and FGF) to promote chondrogenic differentiation and ECM synthesis. The hydrogel matrix network and mechanobiology can be further engineered to mimic the native cartilage by modulating the biomechanics, degradation rate, and porosity via the degree of methacrylation, concentration, and composition ratio. However, several challenges are yet to be addressed such as co-culturing distinct yet interactive cell types, long-term *in-vivo* performance, maturation and scalability of the construct. Advanced platforms such as bioreactors or gradient culture systems are expected to better replicate the native cellular and biophysiochemical interactions. This will enable the investigation of hADSCs and HCs differentiation within a single construct, particularly at the interfaces, utilising co-culture and external stimuli (e.g. fluid flow, growth factors) conditions. Addressing regulatory and ethical concerns is also crucial to ensure safety and accessibility of 3D bioprinted constructs. Clinical collaboration is required to bridge the gap between research and practice. Moreover, the future direction of the field is moving towards personalised treatment, where patient-specific constructs are designed using defect imaging and bioprinting strategies to match the unique anatomical and physiological characteristics of each patient.

Data availability statement

Data will be made available on request.

Acknowledgments

The authors wish to acknowledge the funding provided by the United Kingdom Engineering and Physical Sciences Research Council (EPSRC) Doctoral Prize Fellowship (EP/R513131/1). This work was partially supported by the Henry Royce Institute for Advanced Materials, funded through EPSRC Grants EP/R00661X/1, EP/S019367/1, EP/P025021/1, and EP/P025498/1, as well as by the Nanyang Technological University grant 'Advanced bioprinting strategies for multiscale and multimaterial tissue engineering'.

Author contributions

Yaxin Wang: Conceptualisation, Methodology, Investigation, Validation, Formal analysis, Writing—Original Draft, Writing—Review & Editing, Visualisation. **Yanhao Hou**: Investigation. **Cian Vyas**: Methodology, Validation, Writing—Review & Editing, Supervision, Project administration, Funding acquisition. **Boyang Huang**: Conceptualisation, Methodology, Investigation, Validation, Writing—Review & Editing, Supervision, Project administration. **Paulo Bartolo**: Conceptualisation, Methodology, Validation, Resources, Writing—Review & Editing, Supervision, Project administration, Funding acquisition.

ORCID iDs

Cian Vyas https://orcid.org/0000-0001-6030-1962
Boyang Huang https://orcid.org/0000-0001-5669-349X
Paulo Bartolo https://orcid.org/0000-0003-3683-726X

References

[1] Ansari S, Khorshidi S and Karkhaneh A 2019 Engineering of gradient osteochondral tissue: from nature to lab *Acta Biomater.* **87** 41–54
[2] Wang X *et al* 2022 Identification of an ultrathin osteochondral interface tissue with specific nanostructure at the human knee joint *Nano Lett.* **22** 2309–19
[3] Huey D J, Hu J C and Athanasiou K A 2012 Unlike bone, cartilage regeneration remains elusive *Science* **338** 917–21
[4] Gao F, Xu Z, Liang Q, Li H, Peng L, Wu M, Zhao X, Cui X, Ruan C and Liu W 2019 Osteochondral regeneration with 3D-printed biodegradable high-strength supramolecular polymer reinforced-gelatin hydrogel scaffolds *Adv. Sci.* **6** 1900867
[5] Qiao Z, Lian M, Han Y, Sun B, Zhang X, Jiang W, Li H, Hao Y and Dai K 2021 Bioinspired stratified electrowritten fiber-reinforced hydrogel constructs with layer-specific induction capacity for functional osteochondral regeneration *Biomaterials* **266** 120385
[6] Liu Y *et al* 2021 3D-bioprinted BMSC-laden biomimetic multiphasic scaffolds for efficient repair of osteochondral defects in an osteoarthritic rat model *Biomaterials* **279** 121216
[7] Vyas C, Mishbak H, Cooper G, Peach C, Pereira R F and Bartolo P 2020 Biological perspectives and current biofabrication strategies in osteochondral tissue engineering *Biomanuf. Rev.* **5** 1–24
[8] Wang T *et al* 2022 Repair of osteochondral defects mediated by double-layer scaffolds with natural

osteochondral-biomimetic microenvironment and interface *Mater. Today Bio* **14** 100234
[9] Ding X, Gao J, Yu X, Shi J, Chen J, Yu L, Chen S and Ding J 2022 3D-printed porous scaffolds of hydrogels modified with TGF-β1 binding peptides to promote *in vivo* cartilage regeneration and animal gait restoration *ACS Appl. Mater. Interfaces* **14** 15982–95
[10] Lin D, Cai B, Wang L, Cai L, Wang Z, Xie J, Lv Q-X, Yuan Y, Liu C and Shen S G 2020 A viscoelastic PEGylated poly (glycerol sebacate)-based bilayer scaffold for cartilage regeneration in full-thickness osteochondral defect *Biomaterials* **253** 120095
[11] Gao F *et al* 2018 Direct 3D printing of high strength biohybrid gradient hydrogel scaffolds for efficient repair of osteochondral defect *Adv. Funct. Mater.* **28** 1706644
[12] Dai W, Zhang L, Yu Y, Yan W, Zhao F, Fan Y, Cao C, Cai Q, Hu X and Ao Y 2022 3D bioprinting of heterogeneous constructs providing tissue-specific microenvironment based on host–guest modulated dynamic hydrogel bioink for osteochondral regeneration *Adv. Funct. Mater.* **32** 2200710
[13] Gu Y *et al* 2024 3D-printed biomimetic scaffolds with precisely controlled and tunable structures guide cell migration and promote regeneration of osteochondral defect *Biofabrication* **16** 015003
[14] Wang C *et al* 2020 Cryogenic 3D printing of heterogeneous scaffolds with gradient mechanical strengths and spatial delivery of osteogenic peptide/TGF-β1 for osteochondral tissue regeneration *Biofabrication* **12** 025030
[15] Nowicki M, Zhu W, Sarkar K, Rao R and Zhang L G 2020 3D printing multiphasic osteochondral tissue constructs with nano to micro features via PCL based bioink *Bioprinting* **17** e00066
[16] Chae S, Yong U, Park W, Choi Y-M, Jeon I-H, Kang H, Jang J, Choi H S and Cho D-W 2023 3D cell-printing of gradient multi-tissue interfaces for rotator cuff regeneration *Bioact. Mater.* **19** 611–25
[17] Daly A C and Kelly D J 2019 Biofabrication of spatially organised tissues by directing the growth of cellular spheroids within 3D printed polymeric microchambers *Biomaterials* **197** 194–206
[18] Kilian D, Ahlfeld T, Akkineni A R, Bernhardt A, Gelinsky M and Lode A 2020 3D bioprinting of osteochondral tissue substitutes–*in vitro*-chondrogenesis in multi-layered mineralized constructs *Sci. Rep.* **10** 8277
[19] Vyas C *et al* 2017 3D printing of biocomposites for osteochondral tissue engineering *Biomedical Composites* 2 edn (*Biomaterials*) (Woodhead Publishing) pp 261–302
[20] Bahcecioglu G, Hasirci N, Bilgen B and Hasirci V 2019 A 3D printed PCL/hydrogel construct with zone-specific biochemical composition mimicking that of the meniscus *Biofabrication* **11** 025002
[21] Bahcecioglu G, Bilgen B, Hasirci N and Hasirci V 2019 Anatomical meniscus construct with zone specific biochemical composition and structural organization *Biomaterials* **218** 119361
[22] Luo Y, Cao X, Chen J, Gu J, Yu H, Sun J and Zou J 2022 Platelet-derived growth factor-functionalized scaffolds for the recruitment of synovial mesenchymal stem cells for osteochondral repair *Stem Cells Int.* **2022** 1–15
[23] Zhao Y, Ding X, Dong Y, Sun X, Wang L, Ma X, Zhu M, Xu B and Yang Q 2019 Role of the calcified cartilage layer of an integrated trilayered silk fibroin scaffold used to regenerate osteochondral defects in rabbit knees *ACS Biomater. Sci. Eng.* **6** 1208–16
[24] Jia S *et al* 2018 Multilayered scaffold with a compact interfacial layer enhances osteochondral defect repair *ACS Appl. Mater. Interfaces* **10** 20296–305
[25] Koons G L, Diba M and Mikos A G 2020 Materials design for bone-tissue engineering *Nat. Rev. Mater.* **5** 584–603
[26] Byambaa B *et al* 2017 Bioprinted osteogenic and vasculogenic patterns for engineering 3D bone tissue *Adv. Healthcare Mater.* **6** 1700015
[27] Zhai M, Zhu Y, Yang M and Mao C 2020 Human mesenchymal stem cell derived exosomes enhance cell-free bone regeneration by altering their miRNAs profiles *Adv. Sci.* **7** 2001334
[28] Zha K, Li X, Yang Z, Tian G, Sun Z, Sui X, Dai Y, Liu S and Guo Q 2021 Heterogeneity of mesenchymal stem cells in cartilage regeneration: from characterization to application *npj Regen. Med.* **6** 14
[29] Huang B, Wang Y, Vyas C and Bartolo P 2023 Crystal growth of 3D poly (ε-caprolactone) based bone scaffolds and its effects on the physical properties and cellular interactions *Adv. Sci.* **10** 2203183
[30] Hua Y *et al* 2021 Ultrafast, tough, and adhesive hydrogel based on hybrid photocrosslinking for articular cartilage repair in water-filled arthroscopy *Sci. Adv.* **7** eabg0628
[31] Li P *et al* 2021 Chitosan hydrogel/3D-printed poly (ε-caprolactone) hybrid scaffold containing synovial mesenchymal stem cells for cartilage regeneration based on tetrahedral framework nucleic acid recruitment *Biomaterials* **278** 121131
[32] Yin J, Yan M, Wang Y, Fu J and Suo H 2018 3D bioprinting of low-concentration cell-laden gelatin methacrylate (GelMA) bioinks with a two-step cross-linking strategy *ACS Appl. Mater. Interfaces* **10** 6849–57
[33] Rastin H, Ormsby R T, Atkins G J and Losic D 2020 3D bioprinting of methylcellulose/gelatin-methacryloyl (MC/GelMA) bioink with high shape integrity *ACS Appl. Bio Mater.* **3** 1815–26
[34] Colosi C, Shin S R, Manoharan V, Massa S, Costantini M, Barbetta A, Dokmeci M R, Dentini M and Khademhosseini A 2016 Microfluidic bioprinting of heterogeneous 3D tissue constructs using low-viscosity bioink *Adv. Mater.* **28** 677–84
[35] Li H, Tan Y J, Leong K F and Li L 2017 3D bioprinting of highly thixotropic alginate/methylcellulose hydrogel with strong interface bonding *ACS Appl. Mater. Interfaces* **9** 20086–97
[36] Li H, Tan Y J, Kiran R, Tor S B and Zhou K 2021 Submerged and non-submerged 3D bioprinting approaches for the fabrication of complex structures with the hydrogel pair GelMA and alginate/methylcellulose *Addit. Manuf.* **37** 101640
[37] Lai J, Ye X, Liu J, Wang C, Li J, Wang X, Ma M and Wang M 2021 4D printing of highly printable and shape morphing hydrogels composed of alginate and methylcellulose *Mater. Des.* **205** 109699
[38] Stalling S S, Akintoye S O and Nicoll S B 2009 Development of photocrosslinked methylcellulose hydrogels for soft tissue reconstruction *Acta Biomater.* **5** 1911–8
[39] Loessner D, Meinert C, Kaemmerer E, Martine L C, Yue K, Levett P A, Klein T J, Melchels F P W, Khademhosseini A and Hutmacher D W 2016 Functionalization, preparation and use of cell-laden gelatin methacryloyl–based hydrogels as modular tissue culture platforms *Nat. Protocols* **11** 727
[40] Jones T R, Kang I H, Wheeler D B, Lindquist R A, Papallo A, Sabatini D M, Golland P and Carpenter A E 2008 CellProfiler analyst: data exploration and analysis software for complex image-based screens *BMC Bioinf.* **9** 1–16
[41] McQuin C *et al* 2018 CellProfiler 3.0: next-generation image processing for biology *PLoS Biol.* **16** e2005970
[42] Huang B, Caetano G, Vyas C, Blaker J, Diver C and Bártolo P 2018 Polymer-ceramic composite scaffolds: the effect of

hydroxyapatite and β-tri-calcium phosphate *Materials* **11** 129
[43] Helaehil J V, Lourenço C B, Huang B, Helaehil L V, de Camargo I X, Chiarotto G B, Santamaria-Jr M, Bártolo P and Caetano G F 2021 *In vivo* investigation of polymer-ceramic PCL/HA and PCL/β-TCP 3D composite scaffolds and electrical stimulation for bone regeneration *Polymers* **14** 65
[44] Schwab A, Levato R, D'Este M, Piluso S, Eglin D and Malda J 2020 Printability and shape fidelity of bioinks in 3D bioprinting *Chem. Rev.* **120** 11028–55
[45] Beck E C, Barragan M, Tadros M H, Gehrke S H and Detamore M S 2016 Approaching the compressive modulus of articular cartilage with a decellularized cartilage-based hydrogel *Acta Biomater.* **38** 94–105
[46] Mansour J M 2003 Biomechanics of cartilage *Kinesiology: The Mechanics and Pathomechanics of Human Movement* vol 2 (Lippincott Williams & Wilkins) pp 66–79
[47] Little C J, Bawolin N K and Chen X 2011 Mechanical properties of natural cartilage and tissue-engineered constructs *Tissue Eng.* B **17** 213–27
[48] Chaudhuri O, Gu L, Darnell M, Klumpers D, Bencherif S A, Weaver J C, Huebsch N and Mooney D J 2015 Substrate stress relaxation regulates cell spreading *Nat. Commun.* **6** 1–7
[49] Shah R F, Martinez A M, Pedoia V, Majumdar S, Vail T P and Bini S A 2019 Variation in the thickness of knee cartilage. The use of a novel machine learning algorithm for cartilage segmentation of magnetic resonance images *J. Arthroplasty* **34** 2210–5
[50] Zhou L, Gjvm V O, Malda J, Stoddart M J, Lai Y, Richards R G, Ki-wai Ho K and Qin L 2020 Innovative tissue-engineered strategies for osteochondral defect repair and regeneration: current progress and challenges *Adv. Healthcare Mater.* **9** 2001008
[51] Oláh T, Cucchiarini M and Madry H 2023 Subchondral bone remodeling patterns in larger animal models of meniscal injuries inducing knee osteoarthritis–a systematic review *Knee Surg. Sports Traumatol. Arthrosc.* **31** 5346–64
[52] Morgan E F, Unnikrisnan G U and Hussein A I 2018 Bone mechanical properties in healthy and diseased states *Annu. Rev. Biomed. Eng.* **20** 119–43
[53] Goldstein S A, Wilson D L, Sonstegard D A and Matthews L S 1983 The mechanical properties of human tibial trabecular bone as a function of metaphyseal location *J. Biomech.* **16** 965–9
[54] Morgan E F and Keaveny T M 2001 Dependence of yield strain of human trabecular bone on anatomic site *J. Biomech.* **34** 569–77
[55] Scalzone A, Ferreira A M, Tonda-Turo C, Ciardelli G, Dalgarno K and Gentile P 2019 The interplay between chondrocyte spheroids and mesenchymal stem cells boosts cartilage regeneration within a 3D natural-based hydrogel *Sci. Rep.* **9** 1–12
[56] Kelly T-A N, Roach B L, Weidner Z D, Mackenzie-Smith C R, O'Connell G D, Lima E G, Stoker A M, Cook J L, Ateshian G A and Hung C T 2013 Tissue-engineered articular cartilage exhibits tension–compression nonlinearity reminiscent of the native cartilage *J. Biomech.* **46** 1784–91
[57] Guimarães C F *et al* 2020 The stiffness of living tissues and its implications for tissue engineering *Nat. Rev. Mater.* **5** 351–70
[58] Ouyang L, Armstrong J P K, Lin Y, Wojciechowski J P, Lee-Reeves C, Hachim D, Zhou K, Burdick J A and Stevens M M 2020 Expanding and optimizing 3D bioprinting capabilities using complementary network bioinks *Sci. Adv.* **6** eabc5529
[59] Yue K, Trujillo-de Santiago G, Alvarez M M, Tamayol A, Annabi N and Khademhosseini A 2015 Synthesis, properties, and biomedical applications of gelatin methacryloyl (GelMA) hydrogels *Biomaterials* **73** 254–71
[60] Chansoria P, Asif S, Polkoff K, Chung J, Piedrahita J A and Shirwaiker R A 2021 Characterizing the effects of synergistic thermal and photo-cross-linking during biofabrication on the structural and functional properties of gelatin methacryloyl (GelMA) hydrogels *ACS Biomater. Sci. Eng.* **7** 5175–88
[61] Coughlin M L, Liberman L, Ertem S P, Edmund J, Bates F S and Lodge T P 2021 Methyl cellulose solutions and gels: fibril formation and gelation properties *Prog. Polym. Sci.* **112** 101324
[62] Morozova S 2020 Methylcellulose fibrils: a mini review *Polym. Int.* **69** 125–30
[63] Afghah F, Iyison N B, Nadernezhad A, Midi A, Sen O, Saner Okan B, Culha M and Koc B 2022 3D fiber reinforced hydrogel scaffolds by melt electrowriting and gel casting as a hybrid design for wound healing *Adv. Healthcare Mater.* **11** 2102068
[64] He J *et al* 2023 Gelatin methacryloyl hydrogel, from standardization, performance, to biomedical application *Adv. Healthcare Mater.* **12** 2300395
[65] Yuan X *et al* 2023 Tough gelatin hydrogel for tissue engineering *Adv. Sci.* **10** 2301665
[66] van Velthoven C T J and Rando T A 2019 Stem cell quiescence: dynamism, restraint, and cellular idling *Cell Stem Cell* **24** 213–25
[67] Diamantides N, Dugopolski C, Blahut E, Kennedy S and Bonassar L J 2019 High density cell seeding affects the rheology and printability of collagen bioinks *Biofabrication* **11** 045016
[68] Zhao Y, Li Y, Mao S, Sun W and Yao R 2015 The influence of printing parameters on cell survival rate and printability in microextrusion-based 3D cell printing technology *Biofabrication* **7** 045002
[69] Yamada K M and Sixt M 2019 Mechanisms of 3D cell migration *Nat. Rev. Mol. Cell Biol.* **20** 738–52
[70] Doyle A D, Petrie R J, Kutys M L and Yamada K M 2013 Dimensions in cell migration *Curr. Opin. Cell Biol.* **25** 642–9
[71] Davis T *et al* 2024 How are cell and tissue structure and function influenced by gravity and what are the gravity perception mechanisms? *npj Microgravity* **10** 16
[72] Van Helvert S, Storm C and Friedl P 2018 Mechanoreciprocity in cell migration *Nat. Cell Biol.* **20** 8–20
[73] Lo C-M, Wang H-B, Dembo M and Wang Y-L 2000 Cell movement is guided by the rigidity of the substrate *Biophys. J.* **79** 144–52
[74] Shellard A and Mayor R 2021 Durotaxis: the hard path from *in vitro* to *in vivo Dev. Cell* **56** 227–39
[75] SenGupta S, Parent C A and Bear J E 2021 The principles of directed cell migration *Nat. Rev. Mol. Cell Biol.* **22** 529–47
[76] Zonderland J and Moroni L 2021 Steering cell behavior through mechanobiology in 3D: a regenerative medicine perspective *Biomaterials* **268** 120572
[77] Huebsch N, Arany P R, Mao A S, Shvartsman D, Ali O A, Bencherif S A, Rivera-Feliciano J and Mooney D J 2010 Harnessing traction-mediated manipulation of the cell/matrix interface to control stem-cell fate *Nat. Mater.* **9** 518–26
[78] Lopes D, Martins-Cruz C, Oliveira M B and Mano J F 2018 Bone physiology as inspiration for tissue regenerative therapies *Biomaterials* **185** 240–75

[79] Ortega N, Behonick D J and Werb Z 2004 Matrix remodeling during endochondral ossification *Trends Cell Biol.* **14** 86–93
[80] Aghajanian P and Mohan S 2018 The art of building bone: emerging role of chondrocyte-to-osteoblast transdifferentiation in endochondral ossification *Bone Res.* **6** 19
[81] Lee H-P, Gu L, Mooney D J, Levenston M E and Chaudhuri O 2017 Mechanical confinement regulates cartilage matrix formation by chondrocytes *Nat. Mater.* **16** 1243–51
[82] Huang D, Li Y, Ma Z, Lin H, Zhu X, Xiao Y and Zhang X 2023 Collagen hydrogel viscoelasticity regulates MSC chondrogenesis in a ROCK-dependent manner *Sci. Adv.* **9** eade9497
[83] Liu Y, Shah K M and Luo J 2021 Strategies for articular cartilage repair and regeneration *Front. Bioeng. Biotechnol.* **9** 770655
[84] Murphy C L, Thoms B L, Vaghjiani R J and Lafont J E 2009 Hypoxia. HIF-mediated articular chondrocyte function: prospects for cartilage repair *Arthritis Res. Ther.* **11** 1–7
[85] Markway B D, Cho H and Johnstone B 2013 Hypoxia promotes redifferentiation and suppresses markers of hypertrophy and degeneration in both healthy and osteoarthritic chondrocytes *Arthritis Res. Ther.* **15** 1–14
[86] Demoor M *et al* 2014 Cartilage tissue engineering: molecular control of chondrocyte differentiation for proper cartilage matrix reconstruction *Biochim. Biophys. Acta (BBA)* **1840** 2414–40